Proceedings of ASME Turbo Expo 2011
GT2011
June 6-10, 2011, Vancouver, British Columbia, Canada

GT2011-45814

MINIMISING LOSS IN A HEAT EXCHANGER INSTALLATION FOR AN INTERCOOLED TURBOFAN ENGINE

Pok-Wang Kwan and David R. H. Gillespie
Department of Engineering Science
University of Oxford
Oxford, OX1 3UJ, UK

Rory D. Stieger and Andrew M. Rolt
Strategic Research Centre
Rolls-Royce plc.
Derby, DE24 8BJ, UK

ABSTRACT

An intercooled turbofan engine has been proposed within NEWAC (New Aero Engine Core Concepts, an European Sixth Framework Programme) using lightweight heat exchangers. The requirement for compactness has led to the need for zigzag heat exchanger arrangement where the heat exchanger matrices are inclined to the cooling flows approaching them, but such an arrangement creates non-uniform mass flows through the cold fluid side intercooler ducting and the intercooler heat exchanger matrices. Design guidelines aimed at minimizing aerodynamic losses caused by the flow mal-distribution in such ducting is reported. Minimising the loss has the effect of optimising the heat transfer performance.

Flow velocities and pressure distributions were measured experimentally in a simplified model of a heat exchanger and simulated in Computational Fluid Dynamics (CFD). Good agreement was found between measurement and predictions of the flow distribution in the cold fluid side intercooler ducting downstream of the heat exchanger matrices. A dominant jetting flow in the centre of each exit passage was identified as a source of aerodynamic loss. The CFD simulation has also shown that the main source of aerodynamic loss arises from the severe flow mal-distribution within the heat exchanger matrices.

From these results, design guidelines are presented in this paper for the ducting, based on CFD studies on a series of simplified heat exchanger arrangement geometries.

INTRODUCTION

The potential reduction in Specific Fuel Consumption (SFC) and fuel burn arising from the introduction of intercooling in turbofan engine has been predicted by many researchers [1, 2, 3]. Intercooling could potentially improve the thermal efficiency, and hence the SFC and fuel burn, by increasing the engine Overall Pressure Ratio (OPR) beyond the level achievable in conventional cycle engines. It could also lower the High Pressure (HP) compressor delivery temperature. For a given Turbine Entry Temperature (TET), the increased combustor temperature rise could reduce the core mass flow, and hence core size, required at a given thrust output [3, 4]. The turbine cooling air temperature would also be lowered as it is usually extracted from the HP compressor. This could improve the effectiveness of cooling in turbine components and extend the life of such components.

An intercooled turbofan engine architecture is proposed in the NEWAC programme by Rolls-Royce plc and is described in [4] and also shown in figure 1. The intercooling is carried out between the intermediate (IP) and HP compressor using air from the bypass duct as the heat sink. Major design issues relate to the insertion of the intercooler heat exchanger modules into the core gas path, the transfer of air between the core compressors and the intercooler, the extraction of cooling airflow from the bypass duct, and the performance of the heat exchangers.

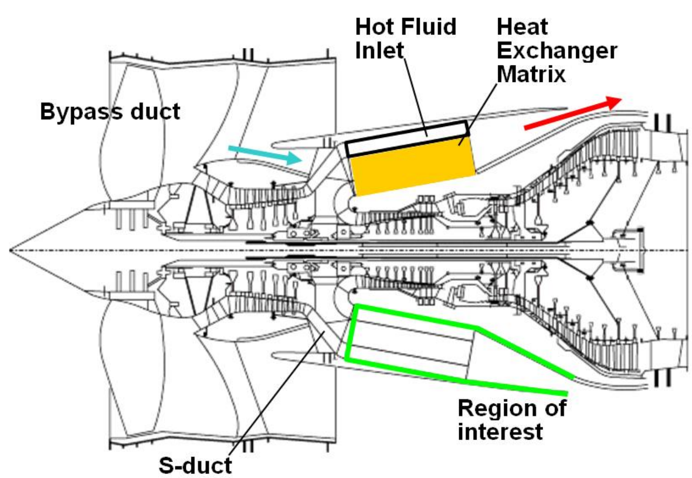

Figure 1: Rolls-Royce intercooled turbofan engine architecture (Courtesy of Rolls-Royce plc.)

Copyright © 2011 by Rolls-Royce plc

The design of the ducting to and from the intercooler hot side was investigated by workers at Loughborough University [5]. The feed ducts from the IP compressor exit to the intercooler are S-shaped ducts. The cold flow enters a region between the upstream faces of the heat exchanger matrices following diffusion from the bypass duct. It is the passage of flow from this point, through the matrices and downstream to the point of reinsertion into the bypass that is the subject of the current study.

Experimental and CFD studies of flow in this general arrangement are presented in the paper. The different configurations modelled are ranked using sensible figures of merit. Thence, design guidelines have been reported here that will enable the aerodynamic installation design of the intercooler heat exchanger modules to be improved.

ENGINE INTERCOOLER INSTALLATION: HEAT EXCHANGERS IN ANNULAR ZIGZAG ARRANGEMENT

In cross-flow heat exchanger matrices heat transfer coefficients drop rapidly moving away from the inlet. Matrices with short passage lengths are thus preferred to designs with longer passages. Short passages are also associated with lower pressure drop. However, to transfer high loads such heat exchangers require a large inlet area.

For the turbofan engine design proposed, the total inlet area required for the cold side of the heat exchangers is greater than the frontal cross-section area around the core available for the installation [3]. It is therefore necessary to angle the heat exchanger units to the inlet flow. A configuration where a series of heat exchanger units is arranged in a zigzag pattern is adopted (Figure 2). The zigzag pattern can be divided into a series of pairs of heat exchanger matrices in V-shaped patterns that create triangular or prismatic regions upstream of each heat exchanger module. The heat exchanger matrix geometry for this study has cross-corrugated primary heat exchange surfaces, which are known to have high volume goodness (VGF, defined in equation 3).

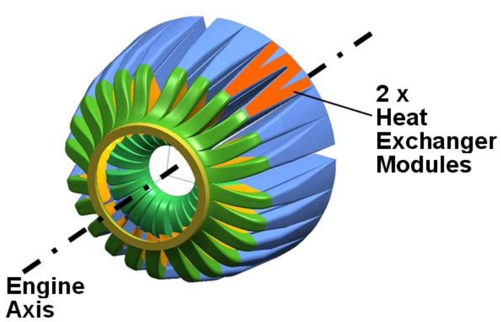

Figure 2: One embodiment of the annular zigzag heat exchanger arrangement around the engine core (Courtesy of Rolls-Royce plc.)

INVESTIGATION STRATEGY

A coupled experimental and CFD strategy was used to assess the value of different flow conditioning schemes in reducing heat exchanger aerodynamic loss in the proposed intercooler application. It was postulated that all the important flow structures present in the annular arrangement would be adequately captured using a single pair of heat exchanger matrices in a plane-sided V-shaped arrangement (Figure 4). Flow and pressure distributions were measured in an experimental study of one such V-shaped arrangement. Here the cross-corrugated passages (or cross-corrugated surface, CCS) (Figure 3, LHS) were explicitly modelled on the cold side of the heat exchanger using corrugated cardboard of the correct pitch to height ratio. The phase of the exits was carefully aligned, and every other passage exit was sealed to ensure a representative flow field (Figure 3, centre).

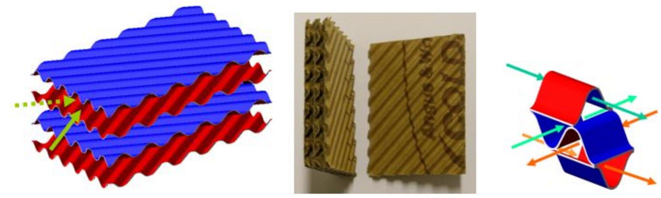

Figure 3: Cross-corrugated heat exchanger matrices, showing the aligned layers of corrugated cardboard used to create the engine scale analogue; a CCS unitary cell.

Several flow conditioning schemes were introduced and the results obtained were used to confirm the general trends in pressure and flow performance. These also provided concrete evidence that the flow conditioning could affect significant benefits.

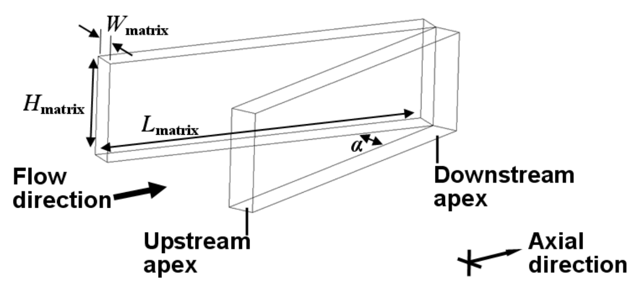

Figure 4: A single pair of heat exchanger matrices in the V-shaped arrangement

More detailed comparison was performed using the results of numerical modelling, as changes to the geometry can be affected with relative ease. Thus results of a CFD study of an engine representative baseline geometry were validated using an experimental test rig (Figure 8) and design variations were then implemented in the CFD study (Figure 7). A total of 11 variants of the representative baseline geometry were compared in CFD. The comparison provides insight into the extent of flow separation and mixing losses, which in turn affect conditions at the exit of the matrix and the velocity profiles downstream.

CFD METHOD

Heat Exchanger Analogue in CFD

To allow the size of the discretised domain to remain manageable in the CFD study, the heat exchanger matrices were

Copyright © 2011 by Rolls-Royce plc

modelled as porous media (for details of this type of fluid zone, see [9]). Setting the flow resistances in the three orthogonal principal directions separately simulated the effects of discrete flow passages. Pressure drop characteristics of the medium were inferred from experimental pressure measurements conducted in a cross-corrugated primary surface (CCS) heat exchanger matrix analogue (Figure 3) and satisfy equation (6). As flow does not pass through the metal surfaces of the matrix, the flow resistance in this direction was set to an arbitrarily high value. The non-flow direction is perpendicular to the orientation of the stacked corrugated layers forming the heat exchanger matrix.

The aim of the current CFD is to model the flow distribution upstream and downstream and through the heat exchanger matrices. Ciofalo et al. [6] found that to resolve the primary heat exchange surfaces for accurate heat transfer prediction requires approximately 88000 elements per unitary cell. Within the current heat exchanger matrix there are >35,000 unitary cells. This made direct prediction of heat transfer coefficient distribution completely unfeasible. An alternative strategy was therefore used to obtain the variation in heat transfer performance. For each flow-conditioning scheme modelled the heat transfer performance could be inferred on a layer by layer basis from existing data in the literature [8], and the predicted through flow velocity. These data were obtained for cross-corrugated surfaces of similar shape, but for large matrices subject to a uniform approach velocity. The overall performance of each heat exchanger installation was then characterised using the figures of merit set out below.

As only the flow distribution was required, it was decided not to solve the energy equation. Unfortunately this also meant that the temperature pick up through the matrix could not be considered, though it is felt that this is a secondary drive of the downstream flow field. Further justification for the use of experimental correlations can be found in [7].

CFD solver and Flow Conditions

The CFD studies were carried out using the commercial solver FLUENT 6.3. ICEM CFD 11 was used for the meshing of the heat exchanger installations. In all cases the meshes were unstructured, using tetrahedral elements throughout, the total number of cells being typically 3 million. y+ values in wall adjacent cells are typically 15. It should be emphasised here that for heat exchange the key purpose of the CFD is not to predict local HTC, but rather to find the matrix through flow distribution for use with existing heat transfer correlations available in the literature. Over the porous medium matrix, the face cell interval less than 1.6 mm. A vertical symmetry planes was created along the tunnel centreline and wall condition was set at the position of the vertical wall of the wind tunnel. Velocity inlet and pressure outlet boundary conditions were imposed to achieve the desired average Reynolds number through the matrices.

Second order discretisation and the realisable *k-ε* turbulence model were used throughout the CFD study. This turbulence model is known to perform well for confined and separating flows, and to produce more accurate results than the standard *k-ε* model [9, 10].

Similar meshing strategies, boundary conditions, and convergence criteria for the CFD simulation were applied throughout the study. A typical example of the mesh resolution is shown for the region close to the heat exchanger in the bottom left hand diagram in figure 5. Here the cell growth ratio is 1.2 from a baseline of a 6 mm interval at the face of the matrix, and is capped at a maximum interval of 25 mm. The resulting mesh has 2,519,437 elements. A finer mesh, used for a grid independence study is also shown in this figure, the outcome is described below.

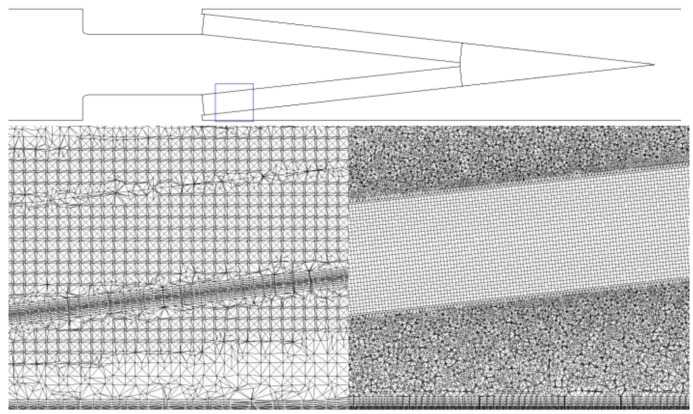

Figure 5: Examples of the typical CFD mesh refinement (left) and a finer mesh used for a grid independence study (right), in a region close to the heat exchanger matrix (top).

The solution was considered converged when the scaled residuals had fallen by three orders of magnitude for momentum and continuity, and importantly were essentially invariant. A typical example is included as figure 6, where second order discretisation is implemented after the first 9000 iterations. Simulations were conducted, in general, on a Dell T7400 PC with 32GB RAM running Windows XP, with satisfactory levels of solution convergence being reached in approximately 36 hours.

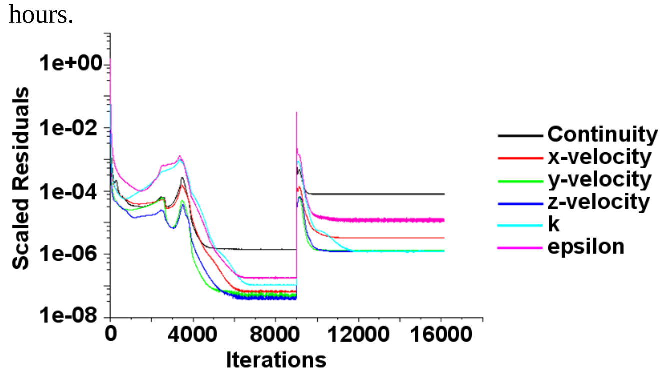

Figure 6:Typical scaled residuals throughout a CFD simulation

Copyright © 2011 by Rolls-Royce plc

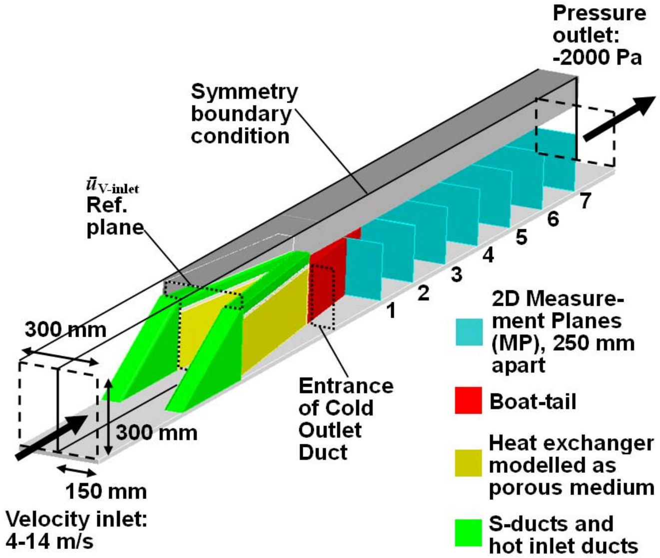

Figure 7: Schematic of Engine representative baseline geometry, showing the general arrangement and measuring planes used in both the CFD campaigns and experimental

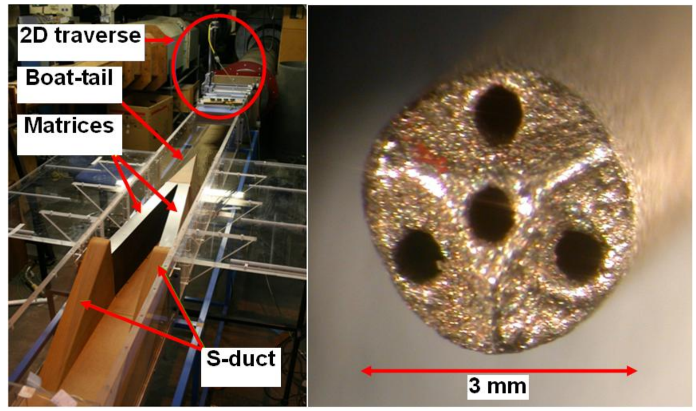

Figure 8: Photograph of the wind tunnel (left) and four-hole probe used in the velocity measurement (right)

The working fluid was air at atmospheric conditions, as this mimicked the air drawn into the inlet of an experimental rig. The flow was considered incompressible. The range of inlet velocity tested in the CFD was 4 - 14 m s^{-1}, which corresponds to Reynolds number tested of $790 > Re > 2600$, where the Reynolds number (Re) is defined in terms of the hydraulic diameter ($D_{h,CCS}$) of a repeating unit cell in the CCS (Figure 3, right) and the area averaged velocity ($\bar{u}_{CCS}$) based on the flow area perpendicular to the mean flow direction. Results were suitably normalised (see figures of merit) to take account in variations in total mass flow rate.

EXPERIMENTAL METHOD

Hydraulic Performance of the Heat Exchanger Analogue

The hydraulic performance of a sample of the CCS matrix (Figure 3) was measured experimentally to provide an empirical correlation for the set up of matrix flow resistance characteristics in the CFD. This measured the static pressure loss is associated with flow approaching normal to the matrix and an unconfined outlet.

Flow Velocity Magnitude Measurement in the Cold Outlet Duct

A photograph of the wind tunnel and the four-hold pyramid probe used for the cold outlet duct flow measurement is shown in figure 8.

The flow velocity magnitude and direction were measured at various axial locations along the cold outlet duct in the wind tunnel indicated in figure 7. The flow was measured using a 3 mm diameter four-hole pyramid probe (Figure 8). The blockage to the wind tunnel flow area is considered insignificant when compared with the flow area of dimensions 300 x 200 mm. The probe was calibrated in subsonic flow with pitch and yaw angles from -40° to 40°.

ENGINE REPRESENTATIVE BASELINE GEOMETRY

The engine representative baseline geometry in the CFD domain and for the experimental set up are shown in Fig. 5. This configuration models the S-ducts and the hot-side inlet manifolds and a plain boat-tail fairing. The S-duct and the hot fluid inlet duct geometry to the heat exchanger are sensibly idealised, while the half-angle of the boat-tail is 6.3°. The initial and maximum width of the boat-tail is equal to the circumferential width of the matrices at their downstream edge.

An engine scale heat exchanger matrix analogue with representative cross-corrugated surfaces was used in the experiment. The overall dimensions of each matrix are 700 x 200 x 55 mm. For the experimental rig and the CFD simulations, an apex angle (Figure 4) of 12.6° was used. This angle is somewhat larger than that proposed for the engine geometry ($<5^{o}$). The arrangement allowed access to the heat exchanger matrices for local flow measurements, whilst maintaining the key loss creating flow features. The (hade) angle of the matrices to the axis of the engine is simulated by a sloped wall directly above the matrices in the V-shaped arrangement (~5°).

Flow developed over a length of 1 m in the 300 x 300 mm cross-sectional area duct prior to flowing between the S-ducts. The total axial extent of the experimental and CFD domains is 4 m. The engine representative baseline geometry was tested at 14 ms^{-1} in the wind tunnel.

Key Flow Structures in the Engine Representative Baseline Installation Geometry

Figure 9 shows the CFD velocity magnitude prediction at the mid-height radial plane of the matrix. This shows the key flow features in the installation: 1) an accelerating flow in the upstream region between the heat exchanger matrices; 2) a

Copyright © 2011 by Rolls-Royce plc

region of fast flow where the outflows from adjacent matrices coalesce downstream of the porous resistance; 3) a separated region behind the downstream apices of the zigzag arrangement. These observation are consistent with to those reported in [11,12].

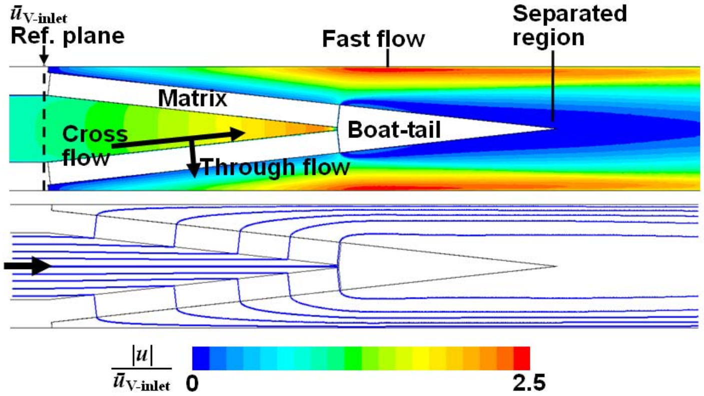

Figure 9: Engine representative baseline geometry CFD mid-height cut plane velocity magnitude contour map and pathlines (Velocity contour within the matrices is re-scaled and shown in Figure 10)

Flow distribution across the face of the matrix

Figure 10, which shows the normalised velocity magnitude distribution at the exit face of the matrix importantly shows flow biased towards the downstream apex. It is worth noting that the velocity distribution is remarkably invariant across the radial height of the matrix, with slight variations near the downstream apex (Figure 10). The slight bias of the flow exiting the matrix towards the inner annulus can be ascribed to the geometry of the inlet S-duct and header (Figure 5). It is important because it causes rotational flow in the cold outlet duct.

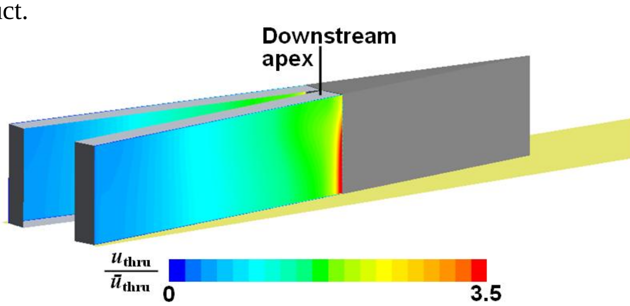

Figure 10: Velocity magnitude distribution at the exit face of the matrix (CFD) normalized by the average through flow velocity

A predominant driver of the flow mal-distribution in the V-shaped arrangement is the pressure gradient required to turn the flow downstream at the exit of the heat exchanger matrices. The ease of turning is determined by the orientation of the flow passages exiting the matrix. In the baseline geometry, the flow exits normal to the face of the heat exchanger. Near the downstream apex there is little pressure gradient to turn the flow axially and it exits with a high velocity transversely across the outlet duct. This acts as a blockage in the passage. Flow exiting the matrices further upstream is then confined to a region midway between the matrices and these flows coalesce into a region of high speed flow. The flow curvature of the exiting flow (Figure 9) causes build up of static pressure towards the upstream apex. The elimination of this transverse velocity through mixing causes addition pressure loss in the system.

There is a sharp increase in the mass flow rate passing though the final 5% of the matrix. This is detrimental to the pressure loss and heat transfer performance. For this simplified engine representative geometry, the drag force on the matrix (and therefore the drag on the coolant extraction system) would be reduced by 42% if flow were uniformly distributed through the matrix.

The extent of downstream separated region

The width of the region occupied by separated flow downstream of the matrix is largely determined by the transverse (circumferential) velocity of the flow exiting the matrices. The slightly higher transverse velocity near the inner annulus of the matrix results in a pair of counter rotating vortices in the cold outlet duct. These sweep fluid down the face of the boat-tail fairing, and cause an increased region of separated flow, near the inner annulus. This is clearly visible in figure 11.

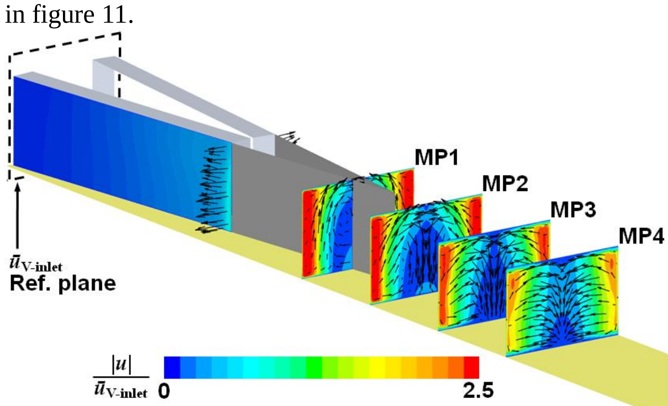

Figure 11: CFD flow velocity contour in cold outlet duct in the engine representative baseline geometry (Vector arrows are indicative and not to a common scale).

In this configuration the flow fails to reattach over the length of the boat-tail fairing near the inner annulus. The separated flow washes out through mixing further downstream. The fast flow at the transverse edge of the flow domain (vertical wind tunnel walls) is clearly visible on all the downstream flow planes. This flow pattern is confirmed by the experimental results (Figure 12). Here the magnitude and direction of reversed flow cannot be resolved but its extent is clear, and the bias towards the inner annulus and extent beyond the end of the boat-tail fairing is clearly visible.

Copyright © 2011 by Rolls-Royce plc

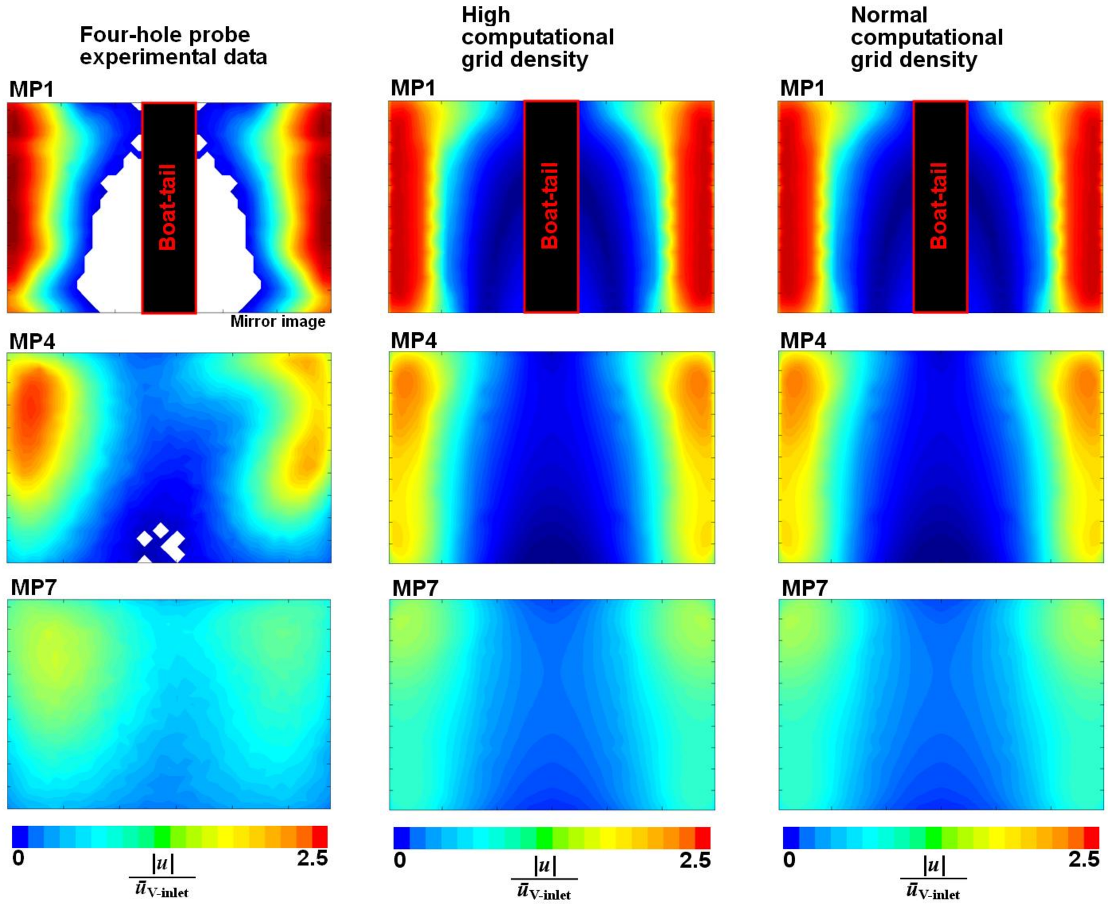

Figure 12: Development of flow in engine representative baseline geometry at measurement planes (MP) 1, 4 & 7 (shown in Figure 4) in the cold side outlet duct; experimental results (left); high grid density CFD results (right) and normal grid density CFD results (right)

The development of the region of fast flow and flow separation in the cold fluid outlet duct are shown in both the experimentally measured and the CFD prediction of dynamic head (Table 1). The non-uniform velocity profile in the cold fluid side outlet exhaust propagates towards the end of the passage. Eliminating the non-uniformity would reduce aerodynamic losses caused by flow mixing in this region.

The contour plots of normalised velocity magnitude in figure 12 show the comparison between experiment and CFD prediction. The velocity magnitude is normalised by the area averaged velocity magnitude at the V-shaped arrangement inlet (Figure 7). As might be expected there is some non-symmetry between the sides in the experimental case, while the CFD has a symmetry plane along its centreline. The size of the separated

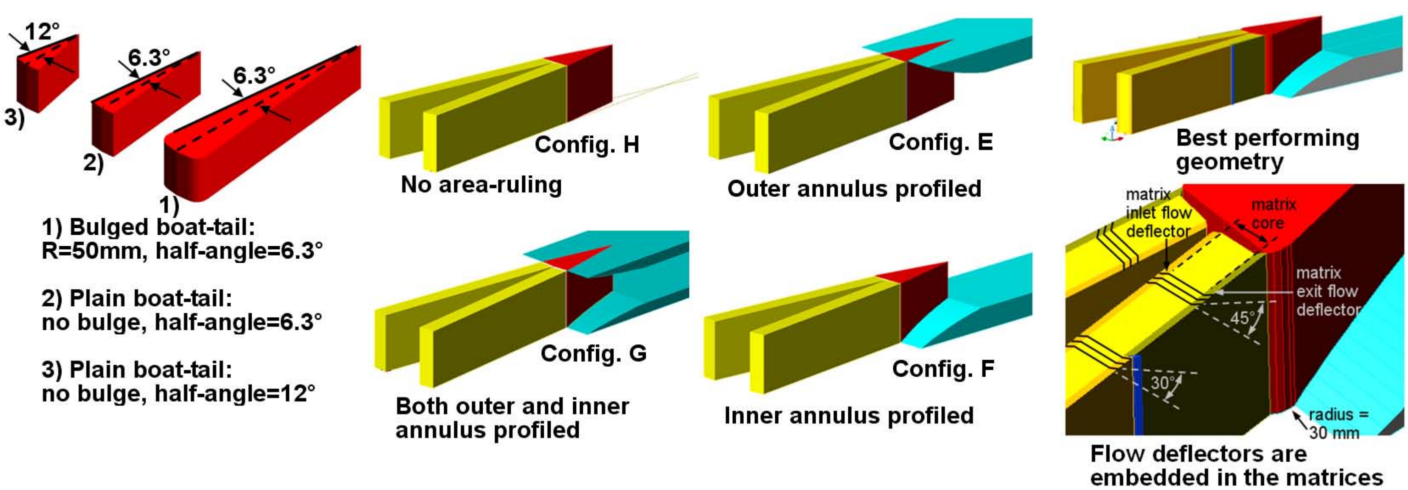

Figure 13: Flow conditioning schemes examples: boat-tail, area-ruling and matrix embedded flow deflectors

Copyright © 2011 by Rolls-Royce plc

region appears to be slightly under predicted in the CFD, but its axial extent is well matched, as is the overall variation of dynamic head across the flow field. In both the experiment and simulation, it is clear that the flow gradually mixes out along the cold fluid side outlet. It is notable that the secondary flows in the regions of highest velocity do not show a pair of passage vortices, but rather a pair of essentially axially flowing jets. It will be shown in the following section that the region of reversed flow can be eliminated using exit flow deflectors or exit turning vanes, and that these are also responsible for improving flow uniformity across the whole passage.

For this geometry the CFD solution can be compared both to experimental results and a CFD solution using a finer mesh. Figure 12 shows comparative results for the normalised velocity distribution at measurement planes 1, 4 and 7 for the experimental, CFD and high density grid CFD results. Considering first the comparison to experimental results the standard deviation in the velocity is found to be 6.1 ms^{-1}. Clearly all the key flow features are well captured including the magnitude of velocity variation. The CFD appears to be poorer at capturing the extent of the mixing in the outlet duct, however, the general agreement allows the CFD to be used as a comparative tool.

For the grid independence study a mesh of 18 million elements was constructed. Here the cell growth ratio is 1.025 from a baseline of a 1.6 mm interval at the face of the matrix, and remains capped at a maximum interval of 25 mm (see Figure 5). In this case a prism layer was attached to all walls of the duct. The porous medium was now implemented as a structured block with higher grid resolution (Figure 5). This was done to ensure minimal numerical diffusion errors as the elements are aligned with the prescribed direction of the flow in this region. The standard deviation in velocity measurements at each plane between the high density mesh CFD and the normal density CFD mesh usually employed was considerably lower than between CFD and experiment lying between 0.79 and 1.3 ms^{-1}. This justifies the meshing strategy employed.

FLOW CONDITIONING SCHEMES

Any flow conditioning scheme applied to the system must allow the installation of banks of heat exchangers of the style described above. While improvement to the heat exchanger corrugated plate surfaces is desirable, the resulting matrix would still be subject to installation losses. The effect on installation loss of the detailed geometry of the cross-corrugated design has not been included in this study. Flow conditioning may be achieved using a combination of geometric features. Amongst these the most promising for this application are the installation of a boat-tail fairing downstream of the heat exchangers; the maintenance of a constant area or contracting duct downstream of the matrices (area-ruling) and the inclusion of flow deflectors in the cooling matrix geometry at its inlet and exit. The aim of the flow conditioning is to remove discontinuities in flow area between discrete matrix exit planes and to reduce flow non-uniformity both within the matrices and in the cold fluid outlet duct. The flow deflectors act as total pressure scoops at the inlet and turn the flow to axial at the exit. Examples of each of these features are shown in figure 13, where they may also be used in combination with one another.

Boat-tail fairings and Area-ruling of the Cold Outlet Duct

Boat-tail fairings potentially are required to reduce flow separation behind the downstream apex of the V-shaped arrangement. Were the flow to exit the matrices in an axial direction, a plain fairing would allow for controlled diffusion of the flow. The incorporation of a bulge into the boat-tail is to match the exit flow direction from the matrices. Here the aim is to employ the Coandă effect to cause flow reattachment onto the boat-tail surface. Flow reattachment is the key requirement to improve the figures of merit (which will be defined in the following section) for the full installation using a boat-tail fairing. Boat-tail fairings with half-angles ranging from 0º (an axially aligned wall extending from the downstream apex of the matrix to the exit of the outlet duct) to 6.3º and 12º were modelled to ascertain their effectiveness.

The method of profiling the annulus line in the engine, or the top and bottom walls of the current models, such that a constant passage cross-sectional area is maintained, is known as area-ruling. This reduces losses in total pressure associated with sudden or overly rapid enlargement of duct area. The outer annulus, inner annulus or both can be profiled according the local constraints of the installation. Area contraction may even be desirable to obtain the required velocity field for re-injection back into the mainstream flow. Tests were carried out with and without area ruling, using both contoured top and bottom walls. In all cases these were designed to maintain a constant area duct.

Embedded flow deflectors at matrix inlet and exit planes

The incorporation of flow deflectors into the matrices' inlet and exit planes is also shown in figure 13. The purpose of the embedded inlet flow deflectors is to reduce the angle through which the flow needs to turn before entering the matrices and the purpose of the embedded exit flow deflectors is to change the matrix outflow angle. This should reduce the transverse (circumferential) velocity of the outflow and promote flow attachment onto the surfaces of the boat-tail fairing.

The means of modelling flow deflectors using CFD is the same as that used to model the matrix: the flow deflectors are modelled as porous resistances. The directions of the principal axes within the porous media are changed to effect the difference. Plane matrices and matrices with regions inclined at 30° and 45° to a normal from the matrix surface were investigated.

All the CFD studies of installation losses investigated have applied flow conditioning to a system incorporating the V-shaped heat exchanger arrangement along with the engine representative S-duct geometry and hot side flow headers. The schematic of such a system is shown in figure 14. Table 1 lists all of the geometries modelled.

Copyright © 2011 by Rolls-Royce plc

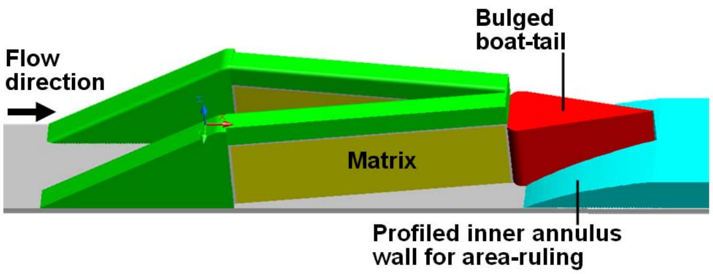

Figure 14: Engine representative geometry with flow conditioning scheme applied in the cold outlet duct

FIGURES OF MERIT FOR COMPARISON OF FLOW CONDITIONING SCHEMES

A good design of heat exchanger installation transfers the required amount heat between the hot and cold streams, with the lowest pressure drop across the system, and returns the spent cooling flow to the mainstream in a manner which is least likely to cause further aerodynamic penalty downstream. In order to assess the performance of the different design schemes tested in this study a number of figures of merit have been defined for the bulk flow as set out below.

Kinetic energy ratio **(KE_{ratio})**

The relationship between heat transfer coefficient (HTC) and mass flow rate generally follows a power law such that:

$$\mathrm{HTC} \propto \dot{m}^{n}. \tag{1}$$

Thence it follows that for a fixed mass flow rate passing through a heat exchanger matrix of fixed geometry the maximum heat transfer occurs when the average flow velocity is as low as possible: i.e. the flow is uniform. To assess flow uniformity, the mass weighted variance of the velocity field normal to the exit plane across the heat exchanger is calculated and normalised by the kinetic energy contained in the same uniform flow. The ratio thus found is a pseudo kinetic energy ratio is used:

$$\mathrm{KE}_{\mathrm{ratio}} = \frac{\int \frac{u_N^2}{2} d\dot{m}_N}{\frac{1}{2}\dot{m}_N \bar{u}_N^2} \tag{2}$$

where u_N is the local flow velocity normal to the plane being analysed, $\bar{u}_N$ is the area averaged normal velocity of the flow whose total mass flow rate is $\dot{m}_N$.

A uniform flow has unity kinetic energy ratio. Higher values are associated with a non-uniform distribution of flow. For a given non-dimensional velocity distribution, the kinetic energy ratio is usefully independent of flow velocity magnitude; and is therefore a robust estimate of flow non-uniformity over a range of inlet velocities (which change with the point in the flight cycle). Results in Table 1 show the kinetic energy ratio at the matrix exit plane, the entrance to the outlet duct (shown in figure 7), and behind the boat-tail fairing.

The kinetic energy ratio defined in equation (2) accounts for the velocity component that contributes to the mass flow rate through the measurement plane, but disregards the kinetic energy associated with the swirling of flow within the measurement plane. Therefore this represents a lower bound to the true value of kinetic energy ratio.

Volume Goodness Factor **(VGF)**

To assess the heat transfer performance of the installation the volume goodness factor has been estimated. This parameter provides a measure of the heat transferred per unit volume per unit pumping power through the heat exchanger. Heat exchanger matrices have high volume goodness factors if they have good heat transfer performance with low aerodynamic penalty. The Volume Goodness Factor (VGF) is defined as:

$$\mathrm{VGF} = \frac{\mathrm{St}}{f^{\frac{1}{3}}} \tag{3}$$

where,

$$\mathrm{St} = \mathrm{Nu}/(\mathrm{Re}\ \mathrm{Pr}) \tag{4}$$

To obtain an estimate of the pumping power required in the system, the Fanning friction factor is required. It is related to

Config.	Area-ruling	Location of profiled wall for area-ruling	Boat-tail half-angle	Boat-tail bulge radius	Inlet flow deflector angle	Exit flow deflector angle	Overall Re	KE_{ratio} at matrix exit plane	KE_{ratio} at entrance of outlet duct	KE_{ratio} at the end of the boat-tail	Overall total pressure drop coefficient	η_{VGF}
Baseline	No	None	6.3°	No bulge	None	None	2606	2.065	2.342	3.903	5.86	**64.3%**
B	No	None	6.3°	R=50mm	None	None	2608	2.044	**1.085**	3.147	5.90	64.5%
C	Yes, non-taped boat-tail straight duct	None	0° non-tapered	No bulge	None	None	901	1.942	1.849	1.572	5.76	65.4%
D	Yes	Top & bottom	6.3°	No bulge	None	None	901	2.035	1.872	1.591	5.75	64.4%
E	Yes	Top	12°	No bulge	None	None	900	1.947	1.874	1.814	5.93	65.4%
F	Yes	Bottom	12°	No bulge	None	None	900	1.944	1.883	1.846	5.85	65.4%
G	Yes	Top & bottom	12°	No bulge	None	None	900	1.946	1.884	1.794	5.81	65.4%
H	No	None	12°	No bulge	None	None	900	1.937	**2.797**	**4.250**	**6.18**	65.5%
I	Yes	Bottom	12°	R=14.5mm	30°	30°	871	1.846	1.523	1.606	5.33	66.1%
J	Yes	Bottom	12°	R=30mm	30°	30°	761	1.775	1.258	**1.274**	5.44	67.1%
Best performing geometry	Yes	Bottom	12°	R=30mm	30°	Two sets: (see Fig. 15) 1) along 75% forward end of matrix: 30°; 2) along 25% rearward end of matrix: 45°.	845	**1.684**	1.342	1.327	**5.11**	**68.1%**

Table 1: Table of flow conditioning schemes and their performance

Copyright © 2011 by Rolls-Royce plc

the pressure drop by the following equation:

$$\Delta p_{\mathrm{mtrx,static}} = \left\{ 4\left(\frac{1}{2}\rho \cdot \bar{u}_{\mathrm{CCS}}^2\right)\frac{L_{\mathrm{strm}}}{D_{\mathrm{h,CCS}}} \right\} f \,. \tag{5}$$

The hydraulic performance of the matrices in the CFD was evaluated using an empirical correlation for Fanning friction factor determined from measurements of pressure drop across a sample of a CCS carried out by the authors (Figure 3). This measured the loss associated with flow approaching normal to the matrix and an unconfined outlet. The friction factor was correlated to Reynolds number as:

$$f = 1.126\ \mathrm{Re}^{-0.1826} \tag{6}$$

over a range of Reynolds number Re = 500 – 5000 [7].

The Nusselt number along the matrix length in the CFD study was calculated using the correlation reported in [8]:

$$\mathrm{Nu} = 0.01648\ \mathrm{Re} + 6.288, \tag{7}$$

valid for $200 > \mathrm{Re} > 1000$. Nu was extrapolated outside of this range for some of the CFD cases.

Volume goodness factor efficiency (η_{VGF})

If the total potential heat transfer during each test or simulation were constant, then the mass mean volume goodness factor could be used to rank performance. It was not possible to achieve this in the current study, and because it may be useful to compare the results to other primary heat exchangers, a revised parameter, the volume goodness factor efficiency is defined as (equations 7-10):

$$\eta_{\mathrm{VGF}} = \frac{\mathrm{VGF_{mean}}}{\mathrm{VGF_{uni}}} \tag{8}$$

where,

$$\mathrm{VGF} = \frac{\mathrm{St}}{f^{\frac{1}{3}}}, \tag{9}$$

$$\mathrm{St}_{\mathrm{HT\ area\ avg}} = \frac{\sum_i^{NoL} \mathrm{St}_i A_{\mathrm{HT},i}}{\sum_i^{NoL} A_{\mathrm{HT},i}}, \tag{10}$$

$$f_{\mathrm{mass\ avg}} = \frac{\frac{1}{\sum_i^{NoL} \dot{m}_i} \sum_i^{NoL} \dot{m}_i \Delta p_{\mathrm{mtrx,static},i}}{\frac{1}{2}\rho u_{\mathrm{CCS,uni}}^2\, 4\frac{L_{\mathrm{mtrx}}}{D_{\mathrm{h,CCS}}}}. \tag{11}$$

This is the ratio of the mean volume goodness factor locally determined on an element by element basis through the matrix to the volume goodness factor calculated for a matrix of equal matrix inlet area with a uniform through flow of equal total mass flow rate. Note that to evaluate the mean volume goodness factor, it is necessary to calculate the average Stanton number (St) and pressure drop appropriately, these being area and mass flow rate averaged parameters respectively. A choice has been made to express the average friction factor using the dynamic head of the average free flow area velocity. This means that the resulting efficiency is then a measure of how effective a flow conditioning design is in achieving the performance of a similar matrix with uniform through flow. A high value, approaching unity, implies better flow conditioning.

Overall total pressure loss coefficient

The overall total pressure drop is the difference in mass weighted total pressure between the V-shaped arrangement inlet plane and furthest measurement plane downstream (plane 7 on figure 7). This is normalised by the average flow dynamic head at the V-shaped arrangement inlet plane, to take variation in overall mass flow rate into account.

FLOW CONDITIONING SCHEMES COMPARISON

The performance of different flow conditioning schemes modelled in CFD, characterised by the kinetic energy ratio, the overall pressure drop coefficient, and the volume goodness factor efficiency is presented in Table 1 and figures 15-17, and discussed below. To quantify the benefit afforded by each flow conditioning scheme, the change in the figure of merit relative to the baseline geometry is assessed.

Boat-tail slope angle

In this section, engine representative configurations C, D, G and H are compared.

From the CFD results the effect of the boat-tail slope angle has been characterised with and without area-ruling. The pressure drop is reduced and flow uniformity far downstream improved when the 6.3° half-angle boat-tail is used (Baseline) compared to a 12° boat-tail (H). The penalty in pressure drop for a steep boat-tail is 5.4% relative to the baseline case. When the angle is reduced to 0° (C), a non-tapered boat-tail, the overall total pressure drop coefficient is lower than that for the shallow half-angle of 6.3°, with an improvement of 1.7% relative to the baseline case. The potential benefit in overall pressure loss of a non-diffusing duct in configuration C over the baseline geometry is partly offset by the increase in the wetted surface area and associated skin friction.

In area-ruled ducts, profiled at both the top and bottom walls, the overall pressure drop performance of the shallow angle boat-tail (D) is 1.0% better than the steeper boat-tail (G) in the CFD tests.

The loss of performance associated with high boat-tail slope angle (12° half-angle) may be reduced by the use of boat-tail bulging and turning vanes, which is discussed in subsequent sections.

The shallow angle boat-tail fairings have slightly worse Volume Goodness Factor efficiency (η_{VGF}) than the steeper boat-tail angles, however, given that these values are merely inferred from literature, these changes of about 1% may be considered insignificant.

Bulged v. plain boat-tail

In this section, engine representative configurations Baseline and B are compared.

A comparison between configuration B, which has the largest radius bulged boat-tail, and the baseline geometry, shows that the use of a bulged boat-tail fairing can increase flow

Copyright © 2011 by Rolls-Royce plc

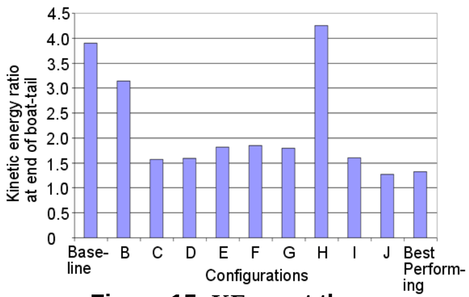

Figure 15: $\mathrm{KE}_{\mathrm{ratio}}$ at the End of Boat-tail

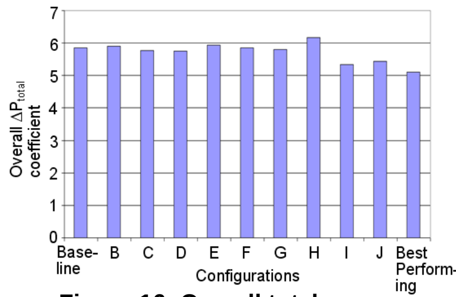

Figure 16: Overall total pressure loss coefficient

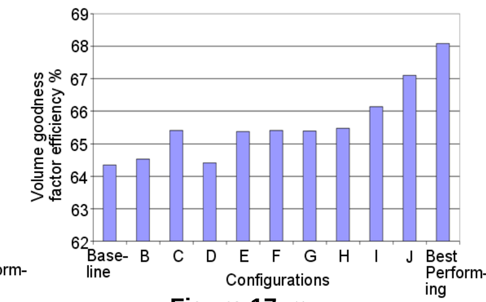

Figure 17: η_{VGF}

uniformity at the entrance to the cold side outlet duct (see Fig. 4). A potential drawback of a bulged boat-tail is that it reduces the cross passage flow area and would result in the undesirable flow acceleration if the flow approached uniformly. Also, for the same boat-tail fairing slope angle, a boat-tail that has a larger bulge is longer due to the increase in its maximum width. So the potential advantage of uniform flow at the cold side outlet duct entrance can be outweighed by flow distortion along the boat-tail surface and increased skin friction due to the acceleration of flow and the lengthening of the boat-tail surface. So while at the cold side outlet duct entrance, this configuration provides the lowest kinetic energy ratio, the kinetic energy ratio at the end of the boat-tail and the overall pressure drop are both higher than that of baseline geometry. Interestingly the low kinetic energy ratio at the entrance to outlet duct did not cause a low kinetic energy ratio at the end of the boat-tail fairing.

When used in combination with flow deflectors at the entrance and the exit of the matrix, and a 12° half-angle boat-tail, increasing the bulge radius is seen to improve all kinetic energy ratios and the volume goodness efficiency in configurations I and J, though the overall pressure drop is very slightly increased.

Area-ruled v. non-area-ruled outlet duct

In this section, engine representative configurations G and H are compared.

Area-ruling is important in limiting the total pressure drop. It is of most additional benefit when used with a steeply angled boat-tail fairing.

When top and bottom wall profiling are added to configuration H to form configuration G, the overall pressure drop coefficient is reduced by 6.3%. The resultant overall pressure drop coefficient for the configuration G (5.81), is better than in the baseline case (5.86). The improvement is much less pronounced (1.9%) when applied to a shallower boat-tail fairing, which inherently has more potential to diffuse the flow.

Thus area-ruling can compensate for the loss in performance associated with a steeper, lighter weight boat-tail.

Profiled top and bottom outlet duct walls

In this section, engine representative configurations E, F and G are compared.

Configuration G which has both top (outer annulus) and bottom (inner annulus) walls profiled has the lowest rate of energy dissipation (rate of drop of total pressure) and overall pressure drop amongst all CFD models which are (a) area-ruled, (b) have 12° boat-tail half-angle and (c) have no turning vanes (configurations E, F, and G). The slope of each of the profiled walls is halved in the configuration G.

The flow velocity near a wall can be manipulated by the curvature of the wall as the flow tends to accelerate in proximity to a convex wall. The position of the jet can then be controlled by profiling the top and the bottom walls as is the case for configurations E, F and G (Figure 18).

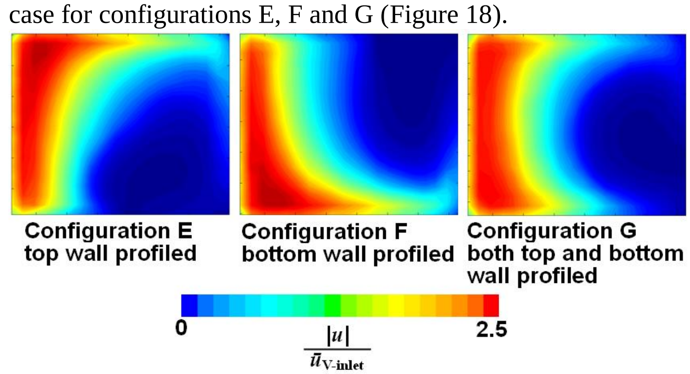

Figure 18: The effect of profiled walls in cold outlet duct: normalised dynamic pressure in CFD results

In configuration E, the velocity magnitude of the flow near the profiled top wall is accelerated, and the jet tends towards the top wall. Similarly, the velocity magnitude is higher in proximity to the profiled surface at the bottom in configuration F; the speed of the jet is similarly increased at the two profiled surfaces in configuration G. When both the top and bottom walls are profiled, the maximum velocity is reduced, and the region of mixing appears also to be lessened, providing a physical explanation of the outcome.

However, it is apparent that the control of jet position is not the most effective way of reducing total pressure drop. Rather, it is to vary the alignment of flow through the heat exchanger towards the free stream direction, using flow deflectors.

Embedded flow deflector at matrix inlet and exit

In this section, engine representative configurations I and J are compared.

This is clearly the most effective method of flow control when combined with other methods. Various Flow deflectors were used with the steep boat-tail fairing, in configurations I, J,

Copyright © 2011 by Rolls-Royce plc

and Best Performing geometry. A carefully designed set of flow deflectors can improve the total pressure drop performance by improving through flow uniformity along the length of the matrix; reducing the transverse (circumferential) velocity component of the matrix outflow by aligning the flow with the axial direction and keeping it attached to the boat-tail surface.

An immediate effect of the reduction of the transverse (circumferential) velocity component at the matrix exit plane is the reduction of the kinetic energy ratio (KE_{ratio}) at the entrance of the outlet duct. The kinetic energy ratios at the entrance of the outlet duct in configurations I, J, and Best Performing geometry are lower than all configurations without flow deflectors except for configuration B which has a 50 mm bulge to promote flow uniformity. However, unlike configuration B, improvements in the overall total pressure loss coefficient and Volume Goodness Factor Efficiency (η_{VGF}) have been recorded (Table 1 and figure 17).

The best flow conditioning scheme:

In this section, the performance of the Best Performing engine representative geometry is discussed.

Of the schemes investigated, the best performance was achieved using the following flow features: a steep boat tail with area ruling using the bottom wall, a moderate boat-tail bulge of radius 30 mm, and inlet and exit flow deflectors as described below. This scheme (Best Performing geometry) has the lowest overall total pressure loss coefficient and the highest Volume Goodness Factor Efficiency (η_{VGF}), with an improvement of 13% and 3.8% respectively over the baseline geometry.

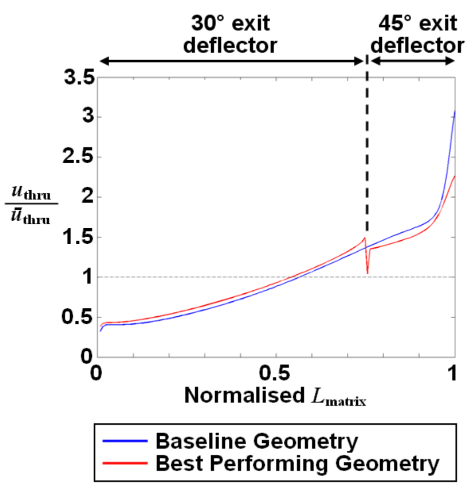

Figure 19: Best Performing Geometry exit flow

It could sensibly be inferred from figure 19 that a major contributor to the low pressure loss is flow uniformity across the exit plane of the matrices: as this reduces the blockage effect at the downstream apex of the matrix. This is indicated by the relatively low KE_{ratio}. On the inlet side of the matrix where the deflector angle is uniform and 30°, the use of flow deflectors reduces the loss associated with the high cross flow near the entrance. On the exit side of the matrices the deflectors were divided into two sections: the exit deflector angle in the forward section of the matrix (near the upstream apex) is 30° and in the rearward section is 45° (shown in Figure 13). The rearward section has a slightly higher flow resistance due to the increase in the angle of deflection.

Figures 19 and 20 shows clearly how the average exit flow distribution is altered if compared to the baseline geometry. The peak through flow velocity u_{thru} is reduced from 3 times the overall all average in the baseline geometry to 2.3 times in the optimised geometry. The kinetic energy ratio at the matrix exit plane is the lowest amongst all configurations tested, being 18% lower than the baseline geometry.

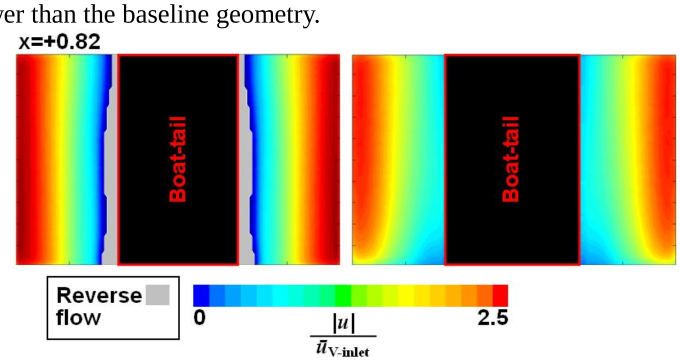

Figure 20: Cold Outlet Duct Entrance Flow Normalised Dynamic Head in Best Performing Geometry

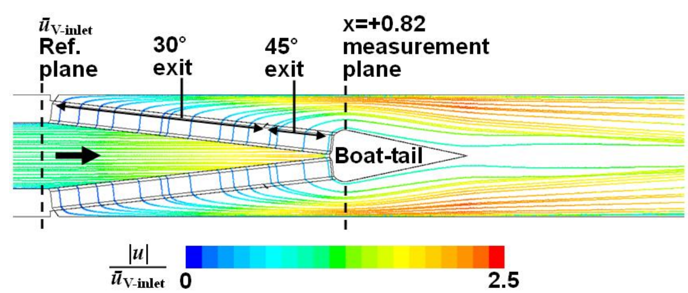

Figure 21: Pathlines in Best Performing Geometry

The overall improvement in performance is evident (in Figure 21) where streamlines through the whole domain at mid-height have been plotted. It is clear that the exit flow remains attached to the surface of the boat-tail (Figures 20 and 21) eliminating the reversed flow region and thus reducing the flow non-uniformity at the end of the boat tail and at the exit of the passage.

CONCLUSION

In this paper, the flow structures in the cold side of a heat exchanger installation for an intercooled turbofan engine are reported. The effectiveness of different flow conditioning strategies, including area-ruling, and of using different shapes of boat-tail fairings and flow deflectors were evaluated. These strategies were applied to a simplified engine representative geometry of the heat exchanger installation and tested using CFD, which was experimentally validated for a baseline case.

Area-ruling reduces the overall pressure loss in the system by 1.9% - 6.3% for the intercooler installation tested. Boat-

Copyright © 2011 by Rolls-Royce plc

tail fairings are always necessary to avoid gross flow separation downstream of the heat exchanger matrices, however, their size must be managed to avoid introducing extra losses due to skin friction and unnecessary flow acceleration. The most significant improvement was observed where matrix embedded flow deflectors were used in combination with an area-ruled outlet duct and moderately bulged boat-tail. The flow deflectors successfully reduce the separation behind the heat exchanger matrices by keeping the flow attached to the boat-tail. Inlet deflectors reduce losses associated with inlet cross flow.

The best performance was observed where the flow resistance of otherwise identical layers of the heat exchanger matrix was altered by varying the angle of deflection of the exit flow along the length of the matrix. This reduced the degree of flow non-uniformity within the matrices by 18%, reducing overall pressure loss by 13% and improving volume goodness by 3.8% relative to the baseline geometry. A means of improving the performance of heat exchanger in the intercooler turbofan engine installation is provided by the research reported in this paper, which could effect the fuel burn benefit achievable in a high OPR engine.

NOMENCLATURE

A_{HT}	Heat transfer area (m^2)
$D_{h,CCS}$	Hydraulic diameter (m) (= 4×Volume/Wetted area of CCS unitary cell)
f	Fanning friction factor
H, L, W	Height, Length, Width (m)
HTC	Heat Transfer Coefficient ($Wm^{-2}K^{-1}$)
$\dot{m}$	Mass flow rate (m/s)
KE_{ratio}	Kinetic energy ratio
L_{mtrx}	Streamwise length of a matrix flow passage layer (m)
NoL	Number of matrix flow passage layers
Nu	Nusselt number
p_{static}, p_{total}	Static pressure, total pressure (Pa)
Pr	Prandtl number
Re	Reynolds number ($=\rho \bar{u}_{thru} D_h / \mu$)
St	Stanton number
$\bar{u}$	Area averaged flow velocity (m/s)
u	Local flow velocity (m/s)
VGF	Volume Goodness Factor
η_{VGF}	Volume Goodness Factor Efficiency
α	Apex angle of V-shaped arrangement
ρ	Flow density (kg m^{-3})
μ	Dynamic viscosity (Pa s)

Subscripts

i	Matrix flow passage layer quantities at the i-th flow layer
mass avg	Mass flow rate averaged
mean	Mean value
mtrx, matrix	Matrix
N	Direction normal to the matrix exit plane
uni	Uniform flow case
thru	Through flow
V-inlet	V-shaped arrangement inlet
HT area avg	Heat Transfer area averaged quantities

ACKNOWLEDGMENTS

The project was funded through E.U. contract number FP6-030876, the funding is gratefully acknowledged. The authors would also like to thank the workshop staff in the Osney Laboratory especially Gerald Walker and Leo Verling who manufactured the experimental facility, and Dr. Noel Morris for his technical discussions.

REFERENCES

[1] Lundbladh, A., and Sjunnesson, A., 2003, "Heat Exchanger Weight and Efficiency Impact on Jet Engine Transport Applications," ISABE 2003 Proceedings, Paper No ISABE-2003-1122.

[2] Xu, L., and Grönstedt, T., 2010, "Design and Analysis of an Intercooled Turbofan Engine," Journal of Engineering for Gas Turbines and Power, 132(11), pp. 114503 (4 pages).

[3] Kyprianidis, K.G., Grönstedt, T., Ogaji, S. O. T., Pilidis. P., and, Singh, R., 2011, "Assessment of Future Aero-engine Designs With Intercooled and Intercooled Recuperated Cores," Journal of Engineering for Gas Turbines and Power, 133(1), pp. 011701 (10 pages).

[4] Rolt, A. M., and Baker, N. J., 2009, "Intercooled Turbofan Engine Design and Technology Research in the EU Framework 6 NEWAC Programme," ISABE 2009 Proceedings, Paper No. ISABE-2009-1278.

[5] Walker, A. D., Carrotte. J. F., and Rolt, A. M., 2009, "Duct Aerodynamics for Intercooled Aero Gas Turbines: Constraints, Concepts and Design Methodology," ASME paper No. GT2009-59612.

[6] Ciofalo, M., Di Piazza, I., and Stasiek, J. A., 2000, “Investigation of flow heat transfer in corrugated-undulated plate heat exchanger,” Heat and Mass Transfer 36, pp 449-462.

[7] Kwan, P. W., 2011, D.Phil. Thesis, University of Oxford, UK

[8] Utriainen, E, and Sundén, B, 2002, “Evaluation of the cross corrugated and some other candidate heat transfer surfaces for microturbine recuperators”, Journal of Engineering for Gas Turbines and Power, 124(3), pp. 550-560.

[9] FLUENT Inc., 2006, "FLUENT 6.3 Users' Guide," FLUENT Inc., Centerra Resource Park, 10 Cavendish Court, Lebanon, NH 03766, USA, Sep 2006.

[10] Shih, T. H., Liou, W. W., Shabbir, A., Yang, Z., and Zhu. J., 1995, "A New k-ε Eddy Viscosity Model for High Reynolds Number Turbulent Flows," Computers & Fluids, 24(3), pp. 227-238.

[11] Mohandes, M. A., 1979, "The Flow Through Heat Exchanger Banks," DPhil Thesis, Department of Engineering Science, University of Oxford.

[12] Moore, F. K., 1979, "Flow Fields and Pressure Losses of V-bundles with Finite Resistance," ASME Paper 79-WA/HT-4, ASME Winter Annual Meeting, December 1979.

Copyright © 2011 by Rolls-Royce plc